condensed matter

MDPI

Article

Single-Band versus Two-Band Description of Magnetism in Infinite-Layer Nickelates

Tharathep Plienbumrung [1,2], Maria Daghofer [1,2], Jean-Baptiste Morée [3,4] and Andrzej M. Oleś [5,*]

1 Institute for Functional Matter and Quantum Technologies, University of Stuttgart, Pfaffenwaldring 57, D-70550 Stuttgart, Germany; maria.daghofer@fmq.uni-stuttgart.de (M.D.)
2 Center for Integrated Quantum Science and Technology, University of Stuttgart, Pfaffenwaldring 57, D-70550 Stuttgart, Germany
3 Waseda Research Institute for Science and Engineering, Waseda University, Shinjuku, Tokyo 169-8555, Japan; jean-baptiste.moree@riken.jp
4 RIKEN Center for Emergent Matter Science, Wako, Saitama 351-0198, Japan
5 Institute of Theoretical Physics, Jagiellonian University, Prof. S. Łojasiewicza 11, 30-348 Kraków, Poland
* Correspondence: a.m.oles@fkf.mpg.de

Abstract: We present a weak-coupling analysis of magnetism in infinite-layer nickelates, where we compare a single-band description with a two-band model. Both models predict that (*i*) hybridization due to hopping is negligible, and (*ii*) the magnetic properties are characterized by very similar dynamic structure factors, $S(\vec{k},\omega)$, at the points $(\pi,\pi,0)$ and (π,π,π). This gives effectively a two-dimensional description of the magnetic properties.

Keywords: high-T_c superconductivity; antiferromagnetism; Mott insulator; entanglement; degenerate Hubbard model; multiband model; random phase approximation

Citation: Plienbumrung, T.; Daghofer, M.; Morée, J.-B.; Oleś, A.M. Single-Band versus Two-Band Description of Magnetism in Infinite-Layer Nickelates. *Condens. Matter* **2023**, *8*, 107. https://doi.org/10.3390/condmat8040107

Academic Editors: Antonio Bianconi and Yasutomo Uemura

Received: 28 October 2023
Revised: 21 November 2023
Accepted: 1 December 2023
Published: 6 December 2023

1. Introduction: Superconducting Infinite-Layer Nickelates $Nd_{1-x}Sr_xNiO_2$

The discovery of Bednorz and Müller [1] marks a new era in the superconductivity research dominated by the search for novel superconductors with high values in the critical temperature T_c. However, in spite of the huge effort in the theory, the mechanism responsible for the pairing in cuprates is still unknown [2], being one of the fundamental open problems in modern condensed matter theory. Perhaps less spectacular was the more recent discovery of superconductivity in infinite-layer $NdNiO_2$ doped by Sr [3], as the values of T_c are here "only" close to 15 K [4]. However, certainly, it attracted more attention to the superconductivity in strongly correlated materials.

The nickelate superconductors are rather similar to cuprate superconductors [5–7]—here also, the two-dimensional (2D) planes of transition metal ions play a central role. At each Ni^+ ion, one has one hole, i.e., d^9 electronic configuration and apical oxygens are absent. Using perturbation theory, such states in a NiO_2 layer give the magnetic short-range order, similar to CuO_2 layer; in cuprates, we even find antiferromagnetic (AFM) long-range order. We find that the charge-transfer gap in a NiO_2 plane is larger than the one in the CuO_2 plane [8–11]. Doped holes reside at oxygen sites in cuprates forming the Zhang–Rice singlet [12]. On the contrary, doped holes likely reside at Ni ions within $Nd_{1-x}Sr_xNiO_2$. This justifies AFM correlations in the one–band model with x^2-y^2 orbitals, which is an effective model of not only superconducting cuprates but also nickelates [5,13]. However, nickelates also need another band that crosses the Fermi energy and is described by a two-band model [14–16]. Here, we present and compare valuable insights from the random phase approximation (RPA), first obtained for cuprates [17].

2. The Two-Band Model and One-Band Model for Infinite-Layer Nickelate

In this paper, we consider (i) a two-orbital Hubbard model and (ii) a one-orbital Hubbard model of infinite-layer nickelate. In (i), the two-orbital model is derived from first

principles and is similar to that in Ref. [15]. The first orbital (denoted as d) is centered on the Ni atom and has antibonding Ni($3d_{x^2-y^2}$)/O($2p_\sigma$) character; the Ni($3d_{x^2-y^2}$) character is dominant. The second orbital (denoted as s) is centered on the Nd atom and has mixed Nd($5d_{3z^2-r^2}$) and interstitial s character; the Nd($5d_{3z^2-r^2}$) character is dominant along the Γ-X-M-Γ path shown in Figure 1, and the interstitial s character is dominant along the Z-R-A-Z path. There is one d orbital and one s orbital per unit cell, and the total filling of both orbitals is one electron. At the DFT level, the occupation number of the nearly half-filled d orbital is 0.91 and that of the nearly empty s orbital is 0.09.

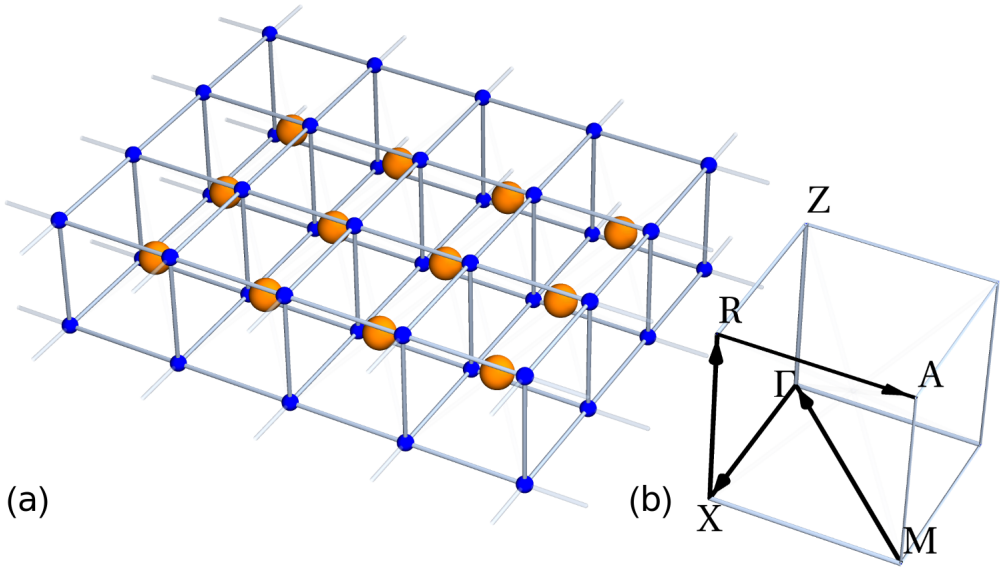

Figure 1. (**a**) Schematic lattice structure of the two-band model for $NiNdO_2$, with Ni(d) blue orbital and Ni(s) orange orbital. The latter orbital is spatially shifted by (0.5, 0.5, 0.5) relative to the Ni(d). (**b**) Brillouin zone used for the two-band model along high-symmetry special points. Special points are: M $\equiv (\pi, \pi, 0)$; Γ $\equiv (0, 0, 0)$; X $\equiv (\pi, 0, 0)$; R $\equiv (\pi, 0, \pi)$; A $\equiv (\pi, \pi, \pi)$; Z $\equiv (0, 0, \pi)$.

The sketch of the model is shown in Figure 1a. To obtain the two-band model, we use the generalized gradient approximation (GGA). The ab initio electronic structure calculations using density functional theory (DFT) were performed employing the QUANTUM ESPRESSO code [18,19] and using a specific choice of pseudopotentials [20]. The computational details are the following: We use the structural data from Ref. [21]. The self-consistent DFT calculation considers a sampling of the full Brillouin zone with an $8 \times 8 \times 8$ $\vec{k}$-point grid and 100 bands. The resulting band structure is used as a starting point for the subsequent calculations.

Then, we perform the Wannier projections by using the RESPACK code [22,23]. The initial guesses for the Wannier orbitals are an $x^2 - y^2$ atomic orbital centered on the Ni atom, and a $3z^2 - r^2$ atomic orbital centered on the Nd atom. To preserve the DFT band dispersion in the Wannier projection, we used an inner window between the Fermi level and +0.7 eV above the Fermi level. Then, we calculate the maximally localized Wannier functions [24,25]. After the calculation, the first orbital d has antibonding Ni($3dx^2 - y^2$)/O($2p_\sigma$) character, and the second orbital s has mixed interstitial s/Nd($5d_{3z^2-r^2}$) character. Finally, we disentangle [26] the other six bands in the band window from the two Wannier bands.

The Hamiltonian of the two-orbital model is

$$\mathcal{H} = H_{dd} + H_{ss} + H_{ds} + H_{\text{int}}. \quad (1)$$

The first three terms in the Hamiltonian (1) stand for the kinetic energy: H_{dd} includes the Ni(d)-Ni(d) hoppings $\propto t^{dd}_{mn}$, H_{ss} includes the Ni(s)-Ni(s) hoppings $\propto t^{ss}_{mn}$, and H_{ds} includes the $d-s$ hybridization $\propto t^{ds}_{mn}$,

$$H_{dd} = \sum_{\{m\mu;n\nu\},\sigma} \left(t^{dd}_{mn} \hat{a}^{\dagger}_{m\alpha\sigma} \hat{a}_{n\nu\sigma} + \text{H.c.} \right), \tag{2}$$

$$H_{ss} = \sum_{\{m\mu;n\nu\},\sigma} \left(t^{ss}_{mn} \hat{a}^{\dagger}_{m\mu\sigma} \hat{a}_{n\nu\sigma} + \text{H.c.} \right), \tag{3}$$

$$H_{ds} = \sum_{\{m\mu;n\nu\},\sigma} \left(t^{ds}_{mn} \hat{a}^{\dagger}_{m\mu\sigma} \hat{a}_{n\nu\sigma} + \text{H.c.} \right), \tag{4}$$

where $\hat{a}^{\dagger}_{m\mu\sigma}$ ($\hat{a}_{n\nu\sigma}$) is the creation (annihilation) operator of an electron at nickel site m in an orbital $\mu \in \{d, s\}$. The hopping parameters t^{mn}_{mn} used in this calculation are set above 0.001 eV, where the three dominant hoppings are: $t^{dd}_{100} = t^{dd}_{010} = 0.369$, $t^{ss}_{002} = 0.286$ and $t^{ss}_{001} = 0.208$ (all in eV). The large kinetic exchange t^{ss}_{00z} along the z-axis is due to its mixing character of Nd$(5d_{3z^2-r^2})$ and the interstitial s. The d-s hybridization is fairly small compared to intra-orbital hoppings. The crystal-field splitting obtained from the Wannier projections is $\epsilon_d = 0.270$ eV and $\epsilon_s = 1.510$ eV, respectively. The Coulomb interaction is as follows [27,28]:

$$H_{\text{int}} = \sum_{m\alpha} U_{\alpha} n_{m\alpha\uparrow} n_{m\alpha\downarrow}, \tag{5}$$

where $\alpha = d, s$ orbitals. $n_{m\mu\sigma}$ is a density operator at site m orbital μ with spin σ. In the two-orbital model, as shown in Figure 1a, the s orbital is spatially shifted by $(0.5, 0.5, 0.5)$. Here, we consider only the on-site Coulomb interaction, i.e., $U_d = 3.26$ eV and $U_s = 0.76$ eV. The calculation of U_d and U_s was carried out by using the constrained random phase approximation (cRPA) [29,30], as implemented in the RESPACK code (details of the cRPA framework can be found in Refs. [22,23]). The computational details are the following: We consider 100 bands, a planewave cutoff energy of 8 Ry for the cRPA polarization and the same $8 \times 8 \times 8$ k-point grid as that in the Wannier projection. The Hund's couplings between the two-orbitals at each site are smaller and are neglected in our two-band model. In (ii), the one-orbital model considers only the d orbital; it is obtained by taking the above-defined effective Hamiltonian for the two-orbital model and removing all effective parameters that involve the s orbital.

3. Results and Discussion

The static structure factor $S(\vec{k})$ (9) is shown in Figure 2 in the PM state at high temperatures along a high-symmetry path through the first Brillouin zone. The results are shown both for the two-band model and for the one-band model defined in Section 2. In the two-band model, the signal coming from the d-band is much stronger than that coming from the s-band, which can already be explained by the different band fillings. Moreover, the modulation is much more pronounced for the d-band, which reflects the stronger correlations in these states. The results for the s-band show quite good agreement with those of the d band.

The structure factor $S(\vec{k})$ is shown along a high-symmetry path, and we have verified that at (π, π, π), i.e., at the A-point, we have indeed found the global maximum. A two-site unit cell can, thus, be expected to capture the magnetic pattern. We, therefore, use a corresponding mean-field *Ansatz* and indeed find a magnetic ordering transition. This does not reflect the physics of infinite-layer nickelate superconductors but is likely an artifact of the mean-field approach used here.

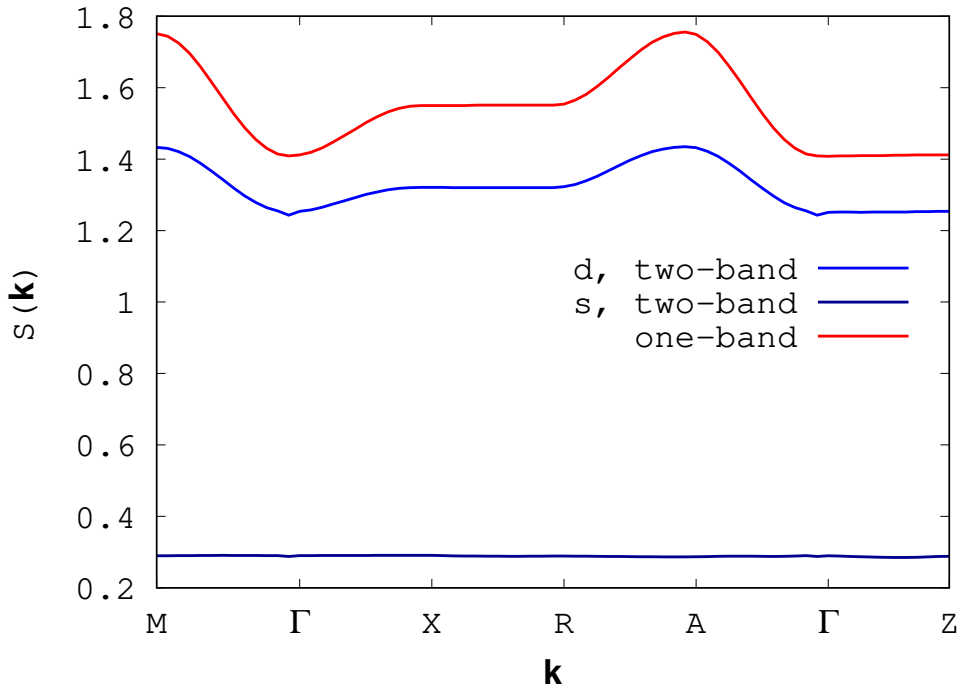

Figure 2. Static spin-structure factor $S(\vec{k})$ for the PM phase at high temperatures for the two-band model (blue and black) and for the one-band model (red). The special points are as in Figure 1.

The structure factor obtained for M = $(\pi, \pi, 0)$ corresponds here to *C*-type magnetic order, i.e., to *C*-AFM order. In contrast, at the A = (π, π, π) point, we find an AFM order of *G*-type, with magnetization alternation in every cubic direction. Both AFM orders are of very similar amplitude. In the uncorrelated two-band model, the M point shows the slightly stronger overall signal; however, the *d*-band prefers the A point already without interaction. When temperature is lowered towards the magnetic transition, the contributions of the *d* states are stronger enhanced, so that the signal at the M point finally dominates. Thus, we conclude that the present models prefer *G*-type alternating magnetic ordering over *C*-type. However, this preference is weak, so that relatively small additions to the present two-band model can be expected to promote *C*-type tendencies. In contrast, the in-plane component of the magnetic correlations is clearly peaked at the M point. The magnetic interactions are, thus, rather 2D in both the two-band and the single-band models. This can be explained by the predominantly in-plane hoppings within the *d*-band.

While the actual materials do not show long-range magnetic order, short-range correlations are present, which the mean-field approximation is unable to capture. Accordingly, magnetic excitations are magnon-like and somewhat similar to those found in cuprates [31,32]. However, the weak-coupling approach used here cannot model localized magnetic moments without long-range magnetic order and this cannot treat short-range magnetic correlations. We, therefore, investigate the ordered state as a proxy for the one with shorter-ranged correlations.

The magnetic excitation spectrum $S(\vec{k}, \omega)$ obtained in the low-temperature AFM phase of the one-band and two-band models are shown in Figures 3 and 4, respectively. We see the magnetic Bragg peak emerge at (π, π, π) and $\omega \to 0$. At $(\pi, \pi, 0)$ and $\omega \approx 0.08$ eV, the high intensity reflects the competing—but loosing—ordering tendency. In addition to these peaks, we find low-energy magnon-like modes with an in-plane dispersion in both models, see Figures 3 and 4. These magnon-like modes are damped, which is likely due to hole doping of the correlated *d* band. Similar models were also observed in experiments at energies $\omega \approx 0.1$ eV [31,32]. There is, thus, good agreement between the experiment and the present one-band model and qualitative agreement with the two-band model.

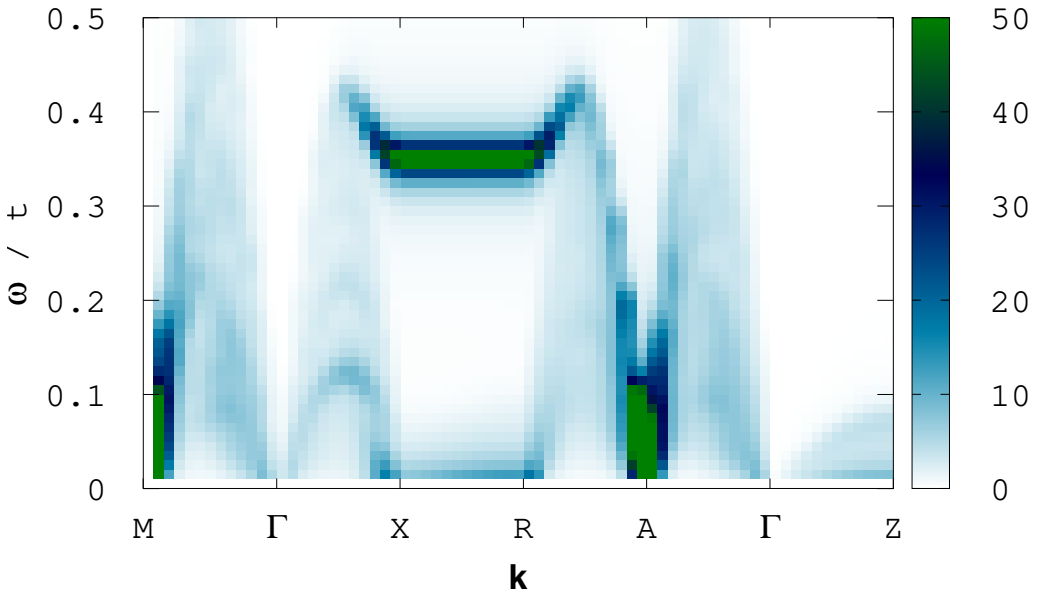

Figure 3. Dynamic spin-structure factor $S(\vec{k}, \omega)$ in the AFM phase of the single-band model, at $\beta = 10$ below the mean-field ordering temperature. Special points as in Figure 1.

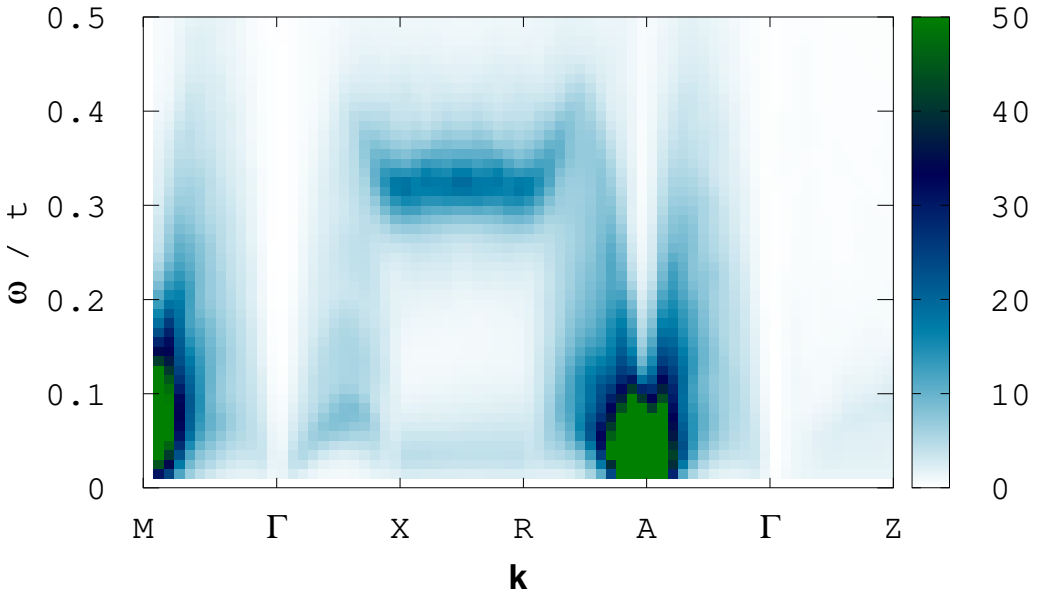

Figure 4. Dynamic spin-structure factor $S(\vec{k}, \omega)$ in the AFM phase of the two-band model at $\beta = 2$ below the mean-field ordering temperature. Special points as in Figure 1. The state is unstable at $\beta = 10$.

The energies of magnetic states are rather close—for instance, DFT using the dynamical mean field theory (DFT+DMFT) approach [33] gives the paramagnetic ground state with the lowest energy, followed by *C*-AFM with energy higher by 20 meV/atom, and *G*-AFM with energy higher by 105 meV/atom. The *C*-AFM state has parallel spins along the *c* axis, while *G*-AFM phase has antiparallel spin alignment to its nearest neighbor in all directions.

Figure 5 shows the band structure of the two-band model. Panel (a) shows uncorrelated bands, which do not depend on temperature. The two colors refer to orbital character, and we see the small hybridization between the bands: Each band is overwhelmingly of one character, with only a little orbital mixing along the Γ-*X* direction. The correlated bands at temperature $T = 0.01$ eV are given in Figure 5b. The correlations broaden both bands in the electronic structure. The *d*-band becomes gapped, while the *s* band remains ungapped

but splits into two along the path shown in the $\vec{k}$-space. Even though magnetic correlations dominate in the d states, the s band also reflects magnetic ordering, and we notice some backfolding of the A = (π, π, π) point towards the Γ-point. The infinite-layer nickelate, thus, combines localized and itinerant aspects.

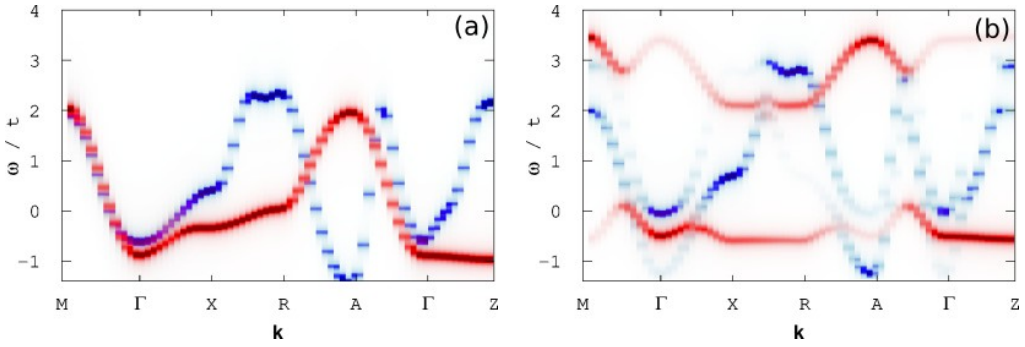

Figure 5. One-particle spectral density $A(\vec{k}, \omega)$ for the two-band model at $\beta = 100$. (**a**) shows results without correlations and (**b**) with on-site interactions included and in the AFM phase. Blue and red refer to the s- and d bands, respectively.

4. Materials and Methods

We discuss here the static and dynamic spin-structure factors, as well as the one-particle Green's functions. The latter are obtained in Hartree–Fock mean-field theory and are for the one-site unit cell above the ordering transition given by the band structure. In a two-site unit cell, where the Brillouin zone is folded in half, we continue to show results for the first Brillouin zone of the one-site unit cell for easier comparison. (This corresponds to the first two Brillouin zones in the reduced-zone scheme.) The orbital-resolved weights' spectral densities are thus given by

$$A^{\alpha}(\vec{k}, \omega) = \sum_{\sigma,\nu} \delta(\omega - \epsilon_{\alpha,\nu,\vec{k}}) \left| \sum_{m} \mathrm{e}^{i\vec{k}\vec{r}_i} u^{\alpha}_{\sigma,\nu,\vec{k},i} \right|^2 . \tag{6}$$

Band ν, spin σ and momentum $\vec{k}$ are good quantum numbers defining the one-electron states in the bands. Component $u^{\alpha}_{\sigma,\nu,\vec{k},m}$ corresponds to orbital $\alpha = s, d$ and then refers to the orbital weight determining the matrix element. Sublattice index m runs over the one or two sites of one unit cell and $\vec{r}_m$ refers to the intra-unit-cell distances.

Magnetism is tracked through transverse spin susceptibilities,

$$\chi^{\mu,\nu}(\vec{k}, i\omega_n) = \frac{1}{N} \int_0^{\beta} \mathrm{d}\tau \, \mathrm{e}^{i\omega_n \tau} \left\langle T_\tau S^+_\mu(\vec{k}, \tau) S^-_\nu(-\vec{k}, \tau) \right\rangle , \tag{7}$$

where μ and ν refer to the orbital, ω_n is the Matsubara frequency, and T_τ is the time-order operator. The spin raising operator

$$S^+_\mu(\vec{k}) = \frac{1}{\sqrt{N}} \sum_{m=1}^{N} \mathrm{e}^{i\vec{k}\vec{r}_m} a^{\dagger}_{m,\alpha,\uparrow} a_{m,\alpha,\downarrow}, \tag{8}$$

and the adjoint $S^-_\nu(-\vec{k})$ are defined as usual, with $a^{\dagger}_{m,\alpha,\sigma}$ ($a_{m,\alpha,\sigma}$) creating (annihilating) an electron with spins σ in orbital $\alpha = s, d$ at site m. The sum runs over all N lattice sites.

Here, we are interested in the static spin-structure factor ($\omega \to 0$), which becomes equivalent to

$$S(\vec{k}) = \sum_{mn} e^{i\vec{k}(\vec{r}_m - \vec{r}_n)} \left\langle \vec{S}_m \cdot \vec{S}_n \right\rangle \tag{9}$$

in an isotropic system, i.e., above the magnetic ordering transition. We also look at the retarded Green's functions describing magnetic excitations, which are given by the analytic continuation of (7), i.e., $(\omega_n \to \omega + i0^+)$.

In order to obtain the susceptibility, we use a multi-orbital implementation of the random-phase approximation (RPA), similar to the approach used in Ref. [34]. However, we replace the 'non-interacting' Green's functions entering the RPA formalism by Hartree–Fock Green's functions, as proposed in [35]. Above the ordering transition, this leads to some Hartree shifts affecting the relative energy of the two bands. This would double-count interactions to some extent, and we fix this by adjusting the crystal-field splitting so that overall band fillings remain similar to those found in DFT. Above the ordering transition, this largely reduces the Hartree–Fock bands to the non-interacting ones. However, we can in this way include magnetically ordered states where bands become different from non-interacting ones. Such an approach has been used to reproduce magnetic excitations observed by inelastic neutron scattering in La_2CuO_4 from a single-band Hubbard model [17]. This previous success in a strongly correlated system leads us to expect insights also for the case of nickelates, even though a weak-coupling treatment may not a priori appear justified.

Finally, we remark on the role played by Nd($4f$) electronic states. We suggest that instead of them, the empty Nd($5d$) orbitals may model the striking electron pocket at the Γ point in the band structure [7]. In such an effective model, the rare-earth atoms are included into Ni atoms via s orbital, indicating the model is three-dimensional, and the Coulomb interaction, as well as Hund's coupling, need to be screened. For instance, the two electrons occupying an s orbital could be located either at Nd or at Ni atom. Therefore, the Coulomb repulsion between these two electrons within the s orbital is reduced. We introduce a parameter $\alpha \in [0, 1]$ to represent the reduced Coulomb interaction and Hund's coupling, i.e., $U_2 = \alpha U_1$ and $J = \alpha J_H$. $\alpha = 1(0)$ stands for the weak (strong) screening effect from rare-earth atoms; more details were given in Ref. [11], and we do not repeat them here. We study the effective two-band model via the Lanczos algorithm [11,36] on a $2 \times 2 \times 2$ unit cell.

5. Summary and Conclusions

In summary, we have investigated and compared magnetism in two effective models for the infinite-layer nickelate superconductor $NdNiO_2$. One model includes both bands found near the Fermi surface, one of d character (with a large $x^2 - y^2$ contribution from Ni ions) and the other one of s character (with large rare-earth weight and centered between Ni ions). We only keep on-site interactions here, which are intra-orbital, since the d and s orbitals are spatially separated here.

We then used a combination of Hartree–Fock mean-field theory and a multi-band multi-site implementation of the random-phase approximation to obtain spectral densities and spin-structure factors. This weak-coupling has been successfully applied to cuprates before [17], suggesting its usefulness here. While it is not able to treat states with short-range magnetic correlations, without long-range order, we were able to infer some tendencies and qualitative aspects of the short-range–correlated state observed in these materials.

We find that ordering vectors A = (π, π, π) and M = $(\pi, \pi, 0)$ closely compete, suggesting that inter-layer couplings are weak. Indeed, this can be rationalized by the fact that magnetic correlations are mostly due to the stronger correlated d bands, which have an almost exclusively 2D band structure, see the band structure on Figure 5. In the ordered state, magnetic excitations show damped in-plane magnon-like modes similar to those observed in infinite-layer nickelates.

Notably, we find here that the one-band and two-band models behave very similarly to each other, with the second band providing basically only self-doping [13]. This can be readily understood from the Hamiltonian, since the bands are only coupled via hopping hybridization, which is very small. A more complete description including long-range Coulomb interactions or coupling to the lattice might change this assessment, however.

Author Contributions: T.P. and M.D. performed the numerical analysis of antiferromagnetic interactions in the two-band model. The two-band model was derived from the multiband model for infinite-layer nickelates by J.-B.M. All authors selected the relevant information, analyzed the predictions of the theory versus the experimental data and developed the interpretation of the numerical results. M.D. and A.M.O. selected the relevant references and wrote the manuscript. All authors have read and agreed to the published version of the manuscript.

Funding: Tharathep Plienbumrung acknowledges Development and Promotion of Science and Technology Talents Project (DPST). Jean-Baptiste Morée acknowledges financial support from the Special Postdoctoral Researcher Program at RIKEN. Andrzej M. Oleś kindly acknowledges Narodowe Centrum Nauki (NCN, National Science Centre, Poland) Project No. 2021/43/B/ST3/02166.

Data Availability Statement: Data available on request.

Acknowledgments: We would like to thank Wojciech Brzezicki, Przemysław Piekarz, George A. Sawatzky and Michael T. Schmid for many insightful discussions. A. M. Oleś is grateful for the Alexander von Humboldt Foundation Fellowship (Humboldt-Forschungspreis).

Conflicts of Interest: We declare no conflict of interest.

References

1. Bednorz, J.G.; Müller, K.A. Possible high-T_c superconductivity in the Ba-La-Cu-O system. *Z. Phys. B* **1986**, *64*, 189–193. [CrossRef]
2. Keimer, B.; Kivelson, S.A.; Norman, M.R.; Uchida, S.; Zaanen, J. From quantum matter to high-temperature superconductivity in copper oxides. *Nature* **2015**, *518*, 179–186. [CrossRef] [PubMed]
3. Li, D.; Lee, K.; Wang, B.Y.; Osada, M.; Crossley, S.; Lee, H.R.; Cui, Y.; Hikita, Y.; Hwang, H.Y. Superconductivity in an infinite-layer nickelate. *Nature* **2019**, *572*, 624–627. [CrossRef] [PubMed]
4. Li, D.; Wang, B.Y.; Lee, K.; Harvey, S.P.; Osada, M.; Goodge, B.H.; Kourkoutis, L.F.; Hwang, H.Y. Superconductiviting Dome in $Nd_{1-x}Sr_xNiO_2$ Infinite Layer Films. *Phys. Rev. Lett.* **2020**, *125*, 027001. [CrossRef]
5. Held, K.; Si, L.; Worm, P.; Janson, O.; Arita, R.; Zhang, Z.; Tomczak, J.M.; Kitatani, M. Phase Diagram of Nickelate Superconductors Calculated by Dynamical Vertex Approximation. *Front. Phys.* **2022**, *9*, 1. [CrossRef]
6. Wu, X.; Di Sante, D.; Schwemmer, T.; Hanke, W.; Hwang, H.Y.; Raghu, S.; Thomale, R. Robust $d_{x^2-y^2}$-wave superconductivity of infinite-layer nickelates. *Phys. Rev. B* **2020**, *101*, 060504(R). [CrossRef]
7. Botana, A.S.; Norman, M.R. Similarities and differences between $LaNiO_2$ and $CaCuO_2$ and implications for superconductivity. *Phys. Rev. X* **2020**, *10*, 011024. [CrossRef]
8. Jiang, M.; Berciu, M.; Sawatzky, G.A. Critical Nature of the Ni Spin State in Doped $NdNiO_2$. *Phys. Rev. Lett.* **2020**, *124*, 207004. [CrossRef]
9. Plienbumrung, T.; Daghofer, M.; Oleś, A.M. Interplay between Zhang-Rice singlet and high-spin states in a model for doped NiO_2 planes. *Phys. Rev. B* **2021**, *103*, 104513. [CrossRef]
10. Plienbumrung, T.; Schmid, M.T.; Daghofer, M.; Oleś, A.M. Character of Doped Holes in $Nd_{1-x}Sr_xNiO_2$. *Condens. Matter* **2021**, *6*, 33. [CrossRef]
11. Plienbumrung, T.; Daghofer, M.; Schmid, M.; Oleś, A.M. Screening in a two-band model for superconducting infinite-layer nickelate. *Phys. Rev. B* **2022**, *106*, 134504. [CrossRef]
12. Zhang, F.C.; Rice, T.M. Effective Hamiltonian for the superconducting Cu Oxides. *Phys. Rev. B* **1988**, *37*, 3759–3761. [CrossRef] [PubMed]
13. Kitatani, M.; Si, L.; Janson, O.; Arita, R.; Zhong, Z.; Held, K. Nickelate superconductors—A renaissance of the one–band Hubbard model. *NPJ Quantum Mater.* **2020**, *5*, 59. [CrossRef]
14. Hu, L.-H.; Wu, C. Two-band model for magnetism and superconductivity in nickelates. *Phys. Rev. Res.* **2019**, *1*, 032046. [CrossRef]
15. Adhikary, P.; Bandyopadhyay, S.; Das, T.; Dasgupta, I.; Saha-Dasgupta, T. Orbital selective superconductivity in a two-band model of infinite-Layer nickelates. *Phys. Rev. B* **2020**, *102*, 100501(R). [CrossRef]
16. Zhang, G.-M.; Yang, Y.F.; Zhang, F.C. Self-doped Mott insulator for parent compounds of nickelate superconductors. *Phys. Rev. B* **2020**, *101*, 020501(R). [CrossRef]
17. Peres, N.M.R.; Araújo, M.A.N. Spin-wave dispersion in La_2CuO_4. *Phys. Rev. B* **2002**, *65*, 132404. [CrossRef]
18. Giannozzi, O.; Baroni, S.; Bonini, N.; Calandra, M.; Car, R.; Cavazzoni, C.; Ceresoli, D.; Chiarotti, G.L.; Cococcioni, M.; Daboet, I.; et al. QUANTUM ESPRESSO: A modular and open-source software project for quantum simulations of materials. *J. Phys. Condens. Matter* **2009**, *21*, 395502. [CrossRef] [PubMed]
19. Giannozzi, O.; Andreussi, O.; Brumme, T.; Bunau, O.; Buongiorno Nardelli, M.; Calandra, M.; Car, R.; Cavazzoni, C.; Ceresoli, D.; Cococcioni, M.; et al. Advanced capabilities for materials modelling with QUANTUM ESPRESSO. *J. Phys. Condens. Matter* **2017**, *29*, 465901. [CrossRef]
20. Dal Corso, A. Pseudopotentials periodic table: From H to Pu. *Comp. Mat. Sci.* **2014**, *95*, 337–350. [CrossRef]
21. Hayward, M.A.; Rosseinsky, M.J. Synthesis of the infinite layer Ni(I) phase $NdNiO_{2+x}$ by low temperature reduction of $NdNiO_3$ with sodium hydride. *Solid State Sci.* **2003**, *5*, 839–850. [CrossRef]

22. Nakamura, K.; Yoshimoto, Y.; Nomura, Y.; Tadano, T.; Kawamura, M.; Kosugi, T.; Yoshimi, K.; Misawa, T.; Motoyama, Y. RESPACK: An ab initio tool for derivation of effective low-energy model of material. *Comp. Phys. Commun.* **2021**, *261*, 107781. [CrossRef]
23. Morée, J.-B.; Hirayama, M.; Schmid, M.T.; Yamaji, Y.; Imada, M. Ab initio low-energy effective Hamiltonians for the high-temperature superconducting cuprates $Bi_2Sr_2CuO_6$, $Bi_2Sr_2CaCu_2O_8$, $HgBa_2CuO_4$, and $CaCuO_2$. *Phys. Rev. B* **2022**, *106*, 235150. [CrossRef]
24. Marzari, N.; Vanderbilt, D. Maximally localized generalized Wannier functions for composite energy bands. *Phys. Rev. B* **1997**, *56*, 12847–12865. [CrossRef]
25. Souza, I.; Marzari, N.; Vanderbilt, D. Maximally localized Wannier functions for entangled energy bands. *Phys. Rev. B* **2001**, *65*, 035109. [CrossRef]
26. Miyake, T.; Aryasetiawan, F.; Imada, M. Ab initio procedure for constructing effective models of correlated materials with entangled band structure. *Phys. Rev. B* **2009**, *80*, 155134. [CrossRef]
27. Oleś, A.M. Antiferromagnetism and correlation of electrons in transition metals. *Phys. Rev. B* **1983**, *28*, 327–339. [CrossRef]
28. Arrigoni, E.; Aichhorn, M.; Daghofer, M.; Hanke, W. Phase diagram and single-particle spectrum of CuO_2 high-T_c layers: Variational cluster approach to the three-band Hubbard model. *New J. Phys.* **2009**, *11*, 055066. [CrossRef]
29. Aryasetiawan, F.; Imada, M.; Georges, A.; Kotliar, G.; Biermann, S.; Lichtenstein, A.I. Frequency-dependent local interactions and low-energy effective models from electronic structure calculations. *Phys. Rev. B* **2004**, *70*, 195104. [CrossRef]
30. Aryasetiawan, F.; Karlsson, K.; Jepsen, O.; Schönberger, U. Calculations of Hubbard U from first-principles. *Phys. Rev. B* **2006**, *74*, 125106. [CrossRef]
31. Lu, H.; Rossi, M.; Nag, M.; Osada, M.; Li, D.F.; Lee, K.; Wang, G.Y.; Garcia-Fernandez, M.; Agrestini, S.; Shen, Z.X.; et al. Magnetic excitations in infinite-layer nickelates. *Science* **2021**, *373*, 213–216. [CrossRef]
32. Lin, J.Q.; Villar Arribi, P.; Fabbris, G.; Botana, A.S.; Meyers, D.; Miao, H.; Shen, Y.; Mazzone, D.G.; Feng, J.; Chiuzbăian, S.G.; et al. Strong superexchange in a $d^{9-\delta}$ nickelate revealed by resonant inelastic x-ray scattering. *Phys. Rev. Lett.* **2021**, *126*, 087001. [CrossRef] [PubMed]
33. Lechermann, F. Doping-dependent character and possible magnetic ordering of $NdNiO_2$. *Phys. Rev. Mater.* **2021**, *5*, 044803. [CrossRef]
34. Graser, S.; Meier, T.A.; Scalapino, D.J. Near-degeneracy of several pairing channels in multiorbital models for the Fe pnictides. *New J. Phys.* **2009**, *11*, 025016. [CrossRef]
35. Brydon, P.M.R.; Daghofer, M.; Timm, C. Magnetic order in orbital models of the iron pnictides. *J. Phys. Condens. Matter* **2011**, *23*, 246001. [CrossRef]
36. Koch, E. The Lanczos Method. In *The LDA+DMFT Approach to Strongly Correlated Materials*; Pavarini, E., Koch, E., Vollhardt, D., Lichtenstein, A., Eds.; Forschungzentrum Jülich: Jülich, Germany, 2011; Volume 1, Chapter 8. ISBN 978-3-89336-734-4.